Surface Science 739 (2024) 122402

Contents lists available at ScienceDirect

Surface Science

journal homepage: www.elsevier.com/locate/susc

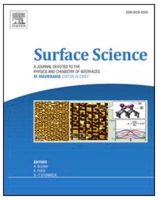

Structural and electronic characterization of Pb adsorption on clean and Cr or Ni doped Fe(1 0 0) surface: An ab-initio study

Simone Giusepponi [a,*], Francesco Buonocore [a], Barbara Ferrucci [b], Massimo Celino [a]

[a] *Italian National Agency for New Technologies, Energy and Sustainable Economic Development (ENEA) - C. R. Casaccia, Via Anguillarese 301, Rome 00123, Italy*
[b] *Italian National Agency for New Technologies, Energy and Sustainable Economic Development (ENEA) - C. R. Bologna, Via Martiri di Monte Sole 4, Bologna 40129, Italy*

ARTICLE INFO

Keywords:
Density Functional Theory DFT
Ab-Initio calculations
Ab-initio characterization
Electronic structure
Iron Fe(1 0 0) surface

ABSTRACT

Using ab-initio calculations, the interaction of lead adatom on both the clean and doped iron (100) surfaces has been investigated. The adsorption energies show that the hollow site provides a more stable configuration with respect to the top and bridge sites, and, in this position, the lead adatom is more energetically favourable than the iron adatom. On the other hand, lead adsorbed in the hollow site of the iron (100) surface doped with chromium, provides more stable system than the nickel doped surfaces with an iron atom adsorbed in the same position. Detailed investigations of inter-layer distances, bonding mechanisms in terms of the projected density of states, magnetic behaviours, and charge density differences are also presented. Our results give insights in the role of the doping the interaction between lead adatom and iron surface, and then, this study may be exploited in the analysis of the corrosion process due to liquid lead.

1. Introduction

Due to their thermo-physical and chemical properties, such as low melting point, high thermal conductivity, and good chemical stability, Heavy Liquid Metal (HLM) alloys, as Pb–Bi eutectic (LBE) are promising materials as primary coolants in the Lead-cooled Fast Reactors (Gen-IV LFRs) and Accelerator Driven Systems (ADSs) proposed for high-level radioactive waste transmutation [1–4].

One of key limiting factors for lead-based alloys usage in LFRs is their high corrosiveness to structural materials, such as ferritic/martensitic steels (e.g., EP823, T91, etc.) and austenitic stainless steels (e.g.,304, 316 L, 15–15Ti, etc.), when in direct contact. At temperatures below 500 °C, a balanced LBE oxygen concentration enables the formation of a self-healing Fe-Cr oxide layer above steel surfaces, acting as a barrier at the lead-steel interface which reduces the corrosion of steel and the release of corrosion products in the HLM. Above 500 °C the oxide layer becomes non-protective, and oxidation or dissolution of steel constituents occur depending on temperature and on oxygen concentration in the liquid metal [2,5–7].

In the last years, thanks to experience gained from studies in nuclear power systems, and due to their high thermal conductivity and chemical stability at temperatures up to 900 °C and above, HLM alloys have also been proposed as advanced high-temperature heat transfer fluids for the next generation of Concentrated Solar Power (CSP) systems to provide increased overall efficiency at reduced specific costs. To increase efficiency, next generation CSP systems will work at higher temperatures ($>$ 1000 °C) and with higher heat fluxes, for this reason Solar Central Receiver Systems (CRS) are considered one of the best choices [8–10]. Lead-Bismuth has a calculated thermal efficiency greater than 90 % [11] and several storage systems, using LBE as storage medium, are investigated to increase the efficiency [12]. However, a technical limit for the adoption of molten lead as a storage material and heat exchange fluid, is represented by the poor corrosion resistance of most commercial Ni-rich high-strength steels, for which a corrosion phenomenon occurs that preferentially attacks the nickel sites contained in the solid solution in structural steels [13].

The so-called liquid-metal corrosion (LMC) phenomena have been investigated in many types of steels in many experimental studies. However, to explore how the liquid atoms deposit onto the surface, and how the deposited atoms affect the escape of iron (Fe) atoms from the steel surface, more detailed knowledge of the atomic-scale physico-chemical processes should be gained. To this end, in this work, we investigated in detail the interaction between lead (Pb) atom and the Fe surface in different configurations using accurate ab-initio

---

* Corresponding author.
E-mail address: simone.giusepponi@enea.it (S. Giusepponi).

https://doi.org/10.1016/j.susc.2023.122402
Received 22 June 2023; Received in revised form 2 October 2023; Accepted 3 October 2023
Available online 5 October 2023

computations. Moreover, the role of lead, chromium and nickel doping is also investigated highlighting that the Ni alloying can hinder the corrosion process due to lead adatom. Although some works have investigated the alloying effect of several elements including Ni [14,15], it has not been clearly stated if Ni can have or not a beneficial effect against the corrosion.

Firstly, we developed a reliable physical model of both Fe-bulk and Fe(100)-surface. To check the ability of the models to reproduce experimental data, ab-initio calculations were performed to obtain lattice parameters, bulk modulus, elastic constants, surface energy and the change of the surface relaxation percentage for the interlayer spacing perpendicular to the clean Fe(100)-surface. Secondly, based on total energy calculations, Pb adsorbed surfaces are investigated by comparing the systems in which a Pb or Fe atom is adsorbed at different sites on the Fe(100) surface. Then, the role played by alloying elements are analysed considering the Fe(100) surface doped with Pb, chromium (Cr), or nickel (Ni) and their effect on the Pb and Fe adatom. For each system the binding energy evaluation is further checked by measuring the interlayer distances and considering the nearest-neighbours analysis. Finally, for each system, the projected density of state (PDOS) is examined to understand how the electronic structure, modified by the composition changes, affects the binding of the adatom. Moreover, the charge density difference and the magnetic behaviour are calculated and analysed.

2. Computational details

Ab-initio calculations based on Density-Functional Theory (DFT) with the Plane-Wave Self-Consistent Field (PWSCF) code were performed using the Quantum ESPRESSO suite [16,17] to accurately characterize the structural and electronic properties of the systems under investigation. PWscf performs different kinds of self-consistent calculations of electronic-structure properties within DFT [18,19] using a Plane-Wave (PW) basis set and Pseudo-Potentials (PP).

The Vanderbilt ultrasoft pseudopotentials [20–22] were used to describe the electron-ion interaction while the exchange-correlation energies were treated with the Perdew-Burke-Ernzerhof (PBE) functional [23] in the generalized gradient approximation (GGA) taking into account the spin polarization. 16, 14, 14 and 18 electrons were explicitly considered in the wave functions for Fe, Pb, Cr and Ni, respectively (semi-core state in valence and scalar relativistic). The electronic wave functions were expanded in a plane-wave basis set with a kinetic energy cut-off of 540 eV (the charge density cut-off was ten times greater) and a k-point mesh of 12 × 12 × 12 Monkhorst-Pack [24] for bulk reference system was employed. Moreover, a Marzari-Vanderbilt smearing [25] with a width of 0.04 Ry was used. All the calculations were performed using the supercell approximation with periodic boundary conditions (PBC) meant to mimic an infinitely extended system.

Preliminary calculations on pseudopotentials were performed to optimize the kinetic energy cut-off, the k sampling, and the smearing width. Total energy, forces and stress were checked with respect to 0.001 Ry/atom, 0.0001 Ry/Bohr and 0.1 Kbar, respectively. The energy minimization was performed by using conjugate gradient (CG) minimization energy method, with a convergence threshold for self-consistency of 10^{-7} Ry. The geometry optimization was performed using the Broyden-Fletcher-Goldfarb-Shanno (BFGS) quasi-newton algorithm. Ionic relaxation was done when the energy changes between two consecutive self-consistent field (SCF) steps was less than 10^{-4} Ry, and the minimal force acting on an atom became less than 5×10^{-4} Ry/Bohr.

The Fe-bulk crystal system is modelled with a 2 × 2 × 2 array of bcc conventional cells (16 atoms). The Fe(100)-surfaces are cleaved from the crystal structure of bcc Fe corresponding to the (100) Miller plane. Experiments have shown that this is the most likely cleavage plane of iron [26]. A vacuum space of 15 Å is inserted in the z-direction to mimic a 2D surface. Such distance has been checked to eliminate the iterations between mirror images in z-direction due to the PBC [27]. To determine the number of layers required to reach convergence for the surface geometry and surface energy, slabs with different number of layers (from 3 up to 15) were modelled. All models used a 2 × 2 crystal unit cell as surface slab in the supercell, with the lattice parameter a_0 calculated from the relaxed bulk system ($L_x = L_y = 2 \times a_0$) and employing a 12 × 12 × 1 Monkhorst-Pack k-point mesh. To achieve the semi-infinite crystal below the surface, all surfaces are optimized by keeping the bottom three layers of atoms fixed. In the surface systems the dipole correction [28] calculation in the vacuum region of the supercell was employed to avoid the artificial electric field associated to the periodic boundary conditions along the z-direction.

To characterize the surface, the surface energy and the percent change of the surface relaxation were calculated [29,30]. The surface energy σ is the energy required to cleave a bulk in two, that is the amount of energy required to create a new surface. This quantity is extracted considering the Fiorentini and Methfessel formula $E^n_{slab} \approx 2\sigma + nE_{bulk}$, where the total energy of the slab systems, E^n_{slab}, depends linearly on the slab thickness (number n of layers) and then σ and E_{bulk} can be extracted from the intercept and slope. Increasing the number of n, the intercept and then σ, tends to an asymptotic value (see the aforementioned references and the discussion therein). Surface relaxation is characterized as the percent change Δ_{ij} of the spacing between layers i and j versus the equilibrium layer spacing d_0.

In addition, the structural analysis of the systems was enriched inspecting the nearest-neighbours (NNs) of the adatom and the atom in position S on the surface.

To quantify the energy required to remove a substitutional atom from a surface, the binding energy, E^s_b, was calculated as:

$$E^s_b = E^s_{slab} - E_{slab+v} - E^s \tag{1}$$

where E^s_{slab} and E_{slab+v} are the energies of the relaxed Fe(100) system with a substitutional atom, and with one missing Fe atom on the surface, respectively; and E^s is the total energy of an isolated substitutional atom. To evaluate the interaction of an added atom (adatom) with the surface, we calculated the binding energy, E^a_b, by using the following equation:

$$E^a_b = E^a_{slab} - E_{slab} - E^a \tag{2}$$

where E^a_{slab} is the total energy of the relaxed Fe(100) system with an adatom on the surface, E_{slab} is the total energy of the relaxed clean surface, and E^a is the total energy of an isolated adatom. A more negative binding energy indicates a more favourable structure. To quantify the energy required to replace one atom of Fe from the surface with an alloying atom, we calculated the formation energy of a defect ΔE, that can be computed by the difference between energy of the system with and without a defect, as follow:

$$\Delta E = \left[E^s_{slab}(Fe) + E^s(Fe)\right] - \left[E_{slab} + E^s\right] \tag{3}$$

where $E^s_{slab}(Fe)$ is the total energy of the relaxed Fe(100) surface with one Fe atom substituted by an alloying atom, E_{slab} and E^s are defined as before. The formation energy of a vacancy on the surface (ΔE_v) was calculated using the following formula:

$$\Delta E_v = E_{slab+v} - E_{slab}[(n-1)/n] \tag{4}$$

where E_{slab+v} and E_{slab} are defined as before and n is the total number of atoms in the slab. A deeper analysis of the action of an adatom/alloying atom on the surface was made calculating the projected density of states (PDOS) of the bulk iron, Fe(100) surface and several adatom/alloying atom on Fe(100) surfaces. The electron charge density (ρ), the difference of the spin-up and -down electron charge densities, i.e. the spin polarization, ($\rho_{up} - \rho_{down}$), and the electron charge densities difference of the adatom + Fe(100) systems ($\rho_{slab+ada} - \rho_{slab} - \rho_{ada}$) were calculated, where the separated systems are kept in the same frozen geometry as the whole system.

3. Bulk and surface model

To ensure the reliability of the model, the lattice parameters, the bulk modulus and elastic constants of crystalline Fe were determined by performing total energy calculations of a 2 × 2 × 2 array bcc conventional cells. Considering the trend of the total energy curve with respect to the side dimension and to the volume of the supercell, the following values of the equilibrium lattice parameter, a_0, and bulk modulus, B, have been derived: $a_0 = 2.866$ Å (eight first NNs (1NNs) at $a_0\sqrt{3}/2 = 2.482$ Å and six second NNs (2NNs) at a_0) and $B = 166$ GPa. Repeating the calculations with a denser k–point mesh (16 × 16 × 16), the same numerical values were obtained. According to the method proposed by Mehl et al. [31], we calculated the following set of elastic constants for bulk iron: $C_{11} = 224$ GPa, $C_{12} = 137$ GPa, and $C_{44} = 89$ GPa. These values clearly satisfy the mechanical stability criterion for the cubic structure, $(C_{11} - C_{12}) > 0$, $(C_{11} + 2C_{12}) > 0$, $C_{11} > 0$ and $C_{44} > 0$. The calculated values are consistent with experimental [32,33] and numerical [34–37] results as reported in Table 1. We also calculated the PDOS for the bulk iron in agreement with other numerical results [38,39]. We found that the ground state is ferromagnetic with total magnetization of 2.45 μB /atom.

For the relaxed Fe(100) clean surface we calculated the surface energy per unit area, $\gamma = \sigma/2A$, where A is the area of the surface unit cell, while the factor of half arises from the 2 free surfaces of the slab; the obtained value, $\gamma = 2.31$ J/m^2, is in good agreement with other theoretical works [35,39–41]. The energetic evaluation is further checked by calculating the binding energy of an Fe atom on the surface $E_b^s(Fe) = -5.02$ (Eq. (1)), and the formation energy of a vacancy on the surface, $\Delta E_v = 0.90$ eV [42] (Eq. (4)).

For this system we evaluated the surface relaxation calculating the percentage change in inter-layer distances, Δ_{ij}, along the direction perpendicular to the surface of systems with an increasing number of layers (from 3 to 15). $\Delta_{ij} = (d_{ij}-d_0)/d_0$, where d_{ij} is the distance between the i^{th} and j^{th} atomic layers after structure relaxation, and d_0 is the interplanar spacing in the bulk, (for the Fe(100) surface $d_0 = a_0/2 = 1.433$ Å). A positive value of Δ_{ij} indicates an expansion, or upwards movement (towards the surface), whereas a negative value indicates a contraction, or downwards displacement (towards the bulk). The results show that a good trade-off between reliable results and computational resources is provided by the Fe(100) surface with 9 layers (36 Fe atoms) for which we found $\Delta_{12} = -3.5$ %, $\Delta_{23} = 2.2$ %, $\Delta_{34} = 0.65$ %, and $\Delta_{45} = 0.13$ % (see Table 2 and Fig. SM1a). Indeed, these results are in very good agreement with experimental data [43,44] and theoretical [39,41,45] studies based on different DFT functionals. Similar expansions/contractions sequences were observed without any significant variations for systems with higher number of layers. Therefore, in the remaining of the present work, the 9 layers slab is used to model the Fe(100) surface. Inspecting the nearest-neighbours of the iron atom on the relaxed surface (see atom in position *S* in Fig. SM2), it was found that there are four 1NNs at 2.45 Å, five 2NNs at 2.86 Å and eight third NNs (3NNs) at 4.04 Å. As expected, due to reduced coordination on the surface, the magnetic state of the system was modified, and the total magnetization of the clean surface is increased from 2.45 (bulk) to 2.65 μB/atom. Moreover, the performed calculations for denser k–point mesh 16 × 16 × 1, given small values of the uncertainty for both the surface energy (< 0.5 mJ/m^2) and relaxation geometries (< 0.1 %). These agreements demonstrate the reliability of our DFT calculations for the surface.

Table 1
Calculated values of the lattice parameter a_0, bulk modulus B and elastic constants C_{11}, C_{12} and C_{44}, compared with experimental [32,33] and numerical [34–36] results.

	a_0 (Å)	B (GPa)	C_{11} (GPa)	C_{12} (GPa)	C_{44} (GPa)
This work	2.866	166	224	137	89
Exp. Ref. [32]	2.866	166	229	134	115
Exp. Ref. [33]		170	240	136	121
Num. Ref. [34]	2.864	173	243	138	122
Num. Ref. [35]	2.831	178	247	143	105
Num. Ref. [36]	2.842	191	274	149	97

Table 2
Percentage change Δ_{ij} in interlayer spacing for clean surface Fe(100) and for clean surface with a vacancy Fe(100)$_{vac}$.

	Fe(100)	Fe(100)$_{vac}$
Δ_{12} (%)	−3.5	−6.4
Δ_{23} (%)	2.2	2.3
Δ_{34} (%)	0.65	0.22
Δ_{45} (%)	0.13	0.12

Taking this as reference model, we calculated the Δ_{ij} for the system Fe(100)$_{vac}$ with one vacancy on the surface. In this case we found: $\Delta_{12} = -6.4$ %, $\Delta_{23} = 2.3$ %, $\Delta_{34} = 0.22$ %, and $\Delta_{45} = 0.12$ % (Fig. SM1b). These values exhibit that a greater contraction of the outer layer occurs with respect to the clean surface. However, the total magnetization of the surface with and without a vacancy is 2.64 μB /atom, almost the same of the clean surface.

4. Energetic and structural analysis of the clean/doped Fe(100) surfaces plus Pb/Fe adatom

4.1. Clean Fe(100) surface plus adatom

To investigate the interaction between lead and the iron surface, using a 9-layers Fe(100) surface as reference model, we studied two systems, indicated as Fe(100)^{Pb} and Fe(100)^{Fe}, in which a Pb adatom and a Fe adatom is adsorbed on the surface, respectively. To this end, three different high-symmetry adsorption sites were considered for the Pb and Fe adatom: on top (T) site directly above a Fe atom, on bridge (B) site between two Fe atoms, and in hollow (H) site in the centre of Fe atoms (see Fig. SM2). Using Eq. (2) we calculated the binding energies of each system. Since a more negative binding energy implies a more favourable structure, the results, reported in Table 3, indicate that Pb and Fe atoms can be stably adsorbed on Fe surface from the liquid phase, and Pb is more stable than Fe. Moreover, for both Fe(100)^{Pb} and Fe(100)^{Fe}, is $E_b^a(\mathrm{H}) < E_b^a(\mathrm{B}) < E_b^a(\mathrm{T}) < 0$. Therefore, the hollow adsorption site represents the most stable configuration, followed by the bridge and top sites. Others numerical calculations report the same stability order for both Pb adatom and for S adatom [14,15,46].

For the six configurations, we calculated the surface relaxation percentage for the interlayer spacing perpendicular to the surface, Δ_{ij} (see Fig. SM3 panels a, b, c for Pb adatom and panels d, e, f for Fe adatom). In

Table 3
Calculated values of the binding energy of the Fe(100) surface with Pb and Fe adatom on three different adsorption sites: top (T), bridge (B) and hollow (H); surface relaxation percentage for the interlayer spacing perpendicular to Fe(100) surface; distances of the Pb and Fe adatoms from the underlying surface; and number (in bold) and distances of the 1NN and 2NN atoms.

	Fe(100)^{Pb}			Fe(100)^{Fe}		
	T	B	H	T	B	H
E_b^a (eV)	−2.83	−3.14	−3.73	−1.68	−2.51	−3.61
Δ_{12} (%)	−1.9	−2.7	−1.5	−0.04	−2.4	−0.30
Δ_{23} (%)	1.7	2.2	1.3	1.4	2.0	1.1
Δ_{34} (%)	0.79	0.80	0.79	1.1	0.85	0.52
Δ_{45} (%)	0.28	0.37	0.17	0.43	0.40	0.42
dist. (Å)	2.42	2.07	1.77	2.08	1.53	1.26
1NN (Å)	**1** (2.52)	**2** (2.65)	**4** (2.78)	**1** (2.15)	**2** (2.25)	**4** (2.39)
2NN (Å)	**4** (3.71)	**2** (3.70)	**1** (3.11)	**4** (3.50)	**2** (3.21)	**1** (2.69)

all cases we found the first layer contracts, while the inner layers expand, and the magnitude of the relaxation is bigger for the first interlayer. Comparing these results with those calculated for the clean Fe (100) (Table 2), we can see the same contraction/expansion sequence occurs. However, the magnitude of the Δ_{12} and Δ_{23} of the six adatom systems tends to be less than the corresponding interlayers of the clean Fe(100) surface, while variations of the remaining interlayers show slightly higher values. All the Δ_{23} values of Fe(100)^{Fe} are slightly smaller than those of Fe(100)^{Pb}. Moreover, we calculated the distance of the adatom from the surface (computed by averaging the heights z of surface atoms, this procedure is always considered hereafter in this work).

As show in Table 3, dist.(T) > dist.(B) > dist.(H) and the Pb values are higher than the corresponding ones for Fe adatom. This is likely due to the larger atomic radius of Pb with respect to Fe.

As a further analysis, we inspected the number and distance of the 1NNs and the 2NNs of the adatoms for Fe(100)^{Pb} and Fe(100)^{Fe} systems. As reported in the Table 3, we found that at the T site, both the adatoms have one 1NN and four 2NNs atoms; at B site the adatom in the two cases has two 1NNs atoms, and two 2NNs atoms; at H site there are four 1NNs and one 2NN atoms.

For the systems with adatom in H site we analysed the surrounding environment of the atom in substitutional *S* position. When the Pb adatom is in H site, the Fe atom in position *S* on the surface has four 1NNs at mean distance of 2.47 Å and six 2NNs at mean distance of 2.85 Å (the Pb adatom at 2.78 Å, two Fe at 2.69 Å, one Fe at 2.86 Å and two Fe at 3.03 Å). When the Fe adatom is in H site, the Fe atom in position *S* on the surface has five 1NNs at mean distance of 2.46 Å (the Fe adatom at 2.39 Å, and four Fe at 2.48 Å) and five 2NNs at 2.86 Å.

4.2. Doped Fe(100) surfaces and doped Fe(100) surfaces plus adatom

In the following, we examine the role of the major alloying elements in steel in doping iron. We considered the three completely relaxed systems in which one (in position *S*) of the Fe-surface atoms is replaced with a lead (Pb), chromium (Cr), or nickel (Ni) atom. In panels a_1, b_1, and c_1 of Fig. SM4, the fully optimized Fe(100)$_{Pb}$, Fe(100)$_{Cr}$, and Fe (100)$_{Ni}$ surfaces are shown and in Table 4 results are reported, respectively. To evaluate the energy required to substitute one Fe-surface atom with an atom of Pb, Cr or Ni, the change in the total energy, ΔE, due to the formation of a defect was calculated (Eq. (3)). We found ΔE (Pb) = 0.11 eV, ΔE (Cr) = 0.90 eV, and ΔE (Ni) = −0.26 eV. Based on these results it should be noted that the Fe(100) surface doped with Ni atom is the only energetically favourable process, while the doping with a Cr or Pb atom requires energy to be provided, especially for Cr.

Using the Eq. (1) we calculated the following values of the binding energy of each substitutional atom on the surface: E_b^s (Pb) = −4.91 eV, E_b^s (Cr) = −4.12 eV, and E_b^s (Ni) = −5.28 eV. These results show that the energy required to remove a Pb, or Cr atom from the surface is slightly lower than the corresponding one for Fe atom on the clean Fe(100) surface (E_b^s (Fe)= −5.02 eV), while is slightly higher in the case of Ni atom.

The comparison between the interlayer percentage relaxation of doped Fe(100) surfaces (Table 4) and the clean Fe(100) surface (Table 3) shows significant differences for the top interlayer variations, and slight differences for the underlying layers variations, especially in case of Fe (100)$_{Pb}$ (the mean z position of the atoms on the surface were considered). Δ_{12} contracts in both Fe(100)$_{Cr}$ and Fe(100)$_{Ni}$, while expands in Fe(100)$_{Pb}$. Indeed, the larger dimension of the Pb atom, compared to the Fe atom, entails a change in the shape of the outer layer, this induces a sharp variation in the percent change of the surface relaxation.

The variations in the number and distances of the 1NNs and 2NNs of the doped atom on the Fe(100)$_{Cr}$ and Fe(100)$_{Ni}$ surfaces remain almost unvaried compared to those observed for the atom in position *S* on the clean Fe(100) surface for which there are four 1NNs at 2.45 Å and five 2NNs at 2.86 Å. Indeed, Cr atom on Fe(100)$_{Cr}$ presents four 1NNs at 2.47 Å and five 2NNs at 2.86 Å, while Ni atom on Fe(100)$_{Ni}$ has four 1NNs at 2.41 Å and five 2NNs: one at 2.78 Å and four at 2.86 Å. The Cr atom is slightly outward from the surface, whereas the Ni atom slightly inward (see panels b_1 and c_1 in Fig. SM4). In contrast, Fe(100)$_{Pb}$ presents the distances of 1NNs and 2NNs atoms stretched with eight 1NNs atoms at a mean distance of 2.94 Å (four atoms at 2.92 Å and four atoms at 2.95 Å), and only one 2NN at 3.59 Å (panels a_1 in Fig. SM4).

The energetic and structural characterizations of doped Fe(100) systems with a Pb or Fe adatom in the hollow site were investigated. The results are reported in Table 4. For both Fe(100)$_{Pb}$ and Fe(100)$_{Cr}$ we found $E_b^{Pb} < E_b^{Fe}$ which means that for these systems the Pb adatom provides a more stable configuration than Fe adatom. However, for both the adatoms, the Fe(100)$_{Cr}$ surface exhibits more negative binding energies than those of Fe(100)$_{Pb}$, with values close to the corresponding ones of the clean Fe(100) surface (see Table 3). Therefore, the Fe and Pb adatom adsorption is more stable on Fe(100)$_{Cr}$ than on Fe(100)$_{Pb}$. For the Fe(100)$_{Ni}$ surface we found $E_b^{Fe} < E_b^{Pb}$, keeping the system with the Fe adatom more stable than that with the Pb adatom.

With respect to the clean Fe(100) surface plus Pb(Fe) adatom in H site, the relaxed Fe(100)$_{Pb}$ surface with Pb(Fe) adatom exhibits an increase of both Δ_{12} and Δ_{23}, this effect is due to the larger dimension of the Pb atom compared to the Fe atom. As for the Fe(100)$_{Cr}$ and Fe(100)$_{Ni}$ surfaces, in which the doping causes a contraction of the outer interlayer of the slabs, also for the systems with adatoms this effect is kept. For Fe (100)$_{Cr}$ and Fe(100)$_{Ni}$ plus Pb(Fe) adatom we found that Δ_{12} is −2.7 (−1.3)% and −3.0(−0.89)%, respectively. These values exhibit an increase of the outer layer contraction compared to that of the Fe(100) surface with Pb(Fe) adatom in H site, for which is Δ_{12} = −1.5(−0.3)%. The remaining Δ_{ij}, as well as the distances of the adatoms from the underlying slab, with changes less than ~0.1 Å, show slight variations with respect to the Fe(100) plus adatom.

In Table 4, the number, and the mean distances of the NNs from adatom are reported. For all the six systems, the Pb(Fe) adatom has four 1NNs and one 2NN, as for the Fe(100) clean surface with Pb(Fe) adatom in H site. With regard to the environment of the substituted atom on the surface, in the Fe(100)$_{Cr}$ with Pb adatom, Cr atom has four 1NNs at a mean distance of 2.48 Å, six 2NNs in the range of 2.70 - 3.02 Å at a mean

Table 4

Calculated values of the binding energy E_b^a of the Pb/Fe adatom in the hollow (H) site on the three different surfaces doped with Pb [Fe(100)$_{Pb}$], Cr [Fe(100)$_{Cr}$], and Ni [Fe(100)$_{Ni}$]. Surface relaxation percentage, Δ_{ij} for the interlayer spacing with and without Pb/Fe adatom. Distances of the Pb/Fe adatom from the underlying surface (in bold), number and distances of the 1NN and the 2NN atoms.

	Fe(100)$_{Pb}$			Fe(100)$_{Cr}$			Fe(100)$_{Ni}$		
Adatom		Pb	Fe		Pb	Fe		Pb	Fe
E_b^a (eV)		−3.19	−2.99		−3.69	−3.63		−3.46	−3.68
Δ_{12} (%)	7.9	9.2	11.8	−4.5	−2.7	−1.3	−4.6	−3.0	−0.89
Δ_{23} (%)	1.9	2.3	1.5	1.9	1.5	0.42	2.1	0.39	1.4
Δ_{34} (%)	0.52	0.68	0.38	0.26	0.78	0.07	0.31	−0.68	0.50
Δ_{45} (%)	0.46	0.82	0.44	−0.05	0.44	−0.07	0.03	−0.93	0.61
dist.(Å)		1.88	1.16		1.81	1.26		1.73	1.24
1NN(Å)		**4**(2.90)	**4**(2.44)		**4**(2.81)	**4**(2.40)		**4**(2.77)	**4**(2.40)
2NN(Å)		**1**(3.44)	**1**(2.74)		**1**(3.12)	**1**(2.67)		**1**(3.04)	**1**(2.64)

distance of 2.87 Å, and with the Pb adatom at 2.89 Å. In the Fe(100)$_{Cr}$ with Fe atom the Cr has five 1NNs in the range of 2.38 - 2.51 Å at a mean distance 2.46 Å, and with the Fe adatom at 2.38 Å and five 2NNs at a mean distance 2.86 Å. In the Fe(100)$_{Ni}$ systems with Pb adatom, Ni atom has four 1NNs at a mean distance 2.44 Å and six 2NNs in the range of 2.62 - 3.10 Å at a mean distance of 2.82 Å and with the Pb adatom at 2.67 Å; in the Fe(100)$_{Ni}$ systems with Fe adatom, Ni atom has five 1NNs in the range of 2.34 - 2.45 Å at a mean distance 2.42 Å and with the Fe adatom at 2.34 Å and five 2NNs at a mean distance 2.82 Å.

Due to the size of the Pb atom, the analysis of the Fe(100)$_{Pb}$ surfaces is more complex. The Pb atom on the surface has nine 1NNs in the range of 2.83 - 3.09 Å at a mean distance of 2.96 Å, two 2NNs at a mean distance of 3.76 Å, and with the Pb adatom at 3.04 Å. Similar results are found for the Fe adatom. The Pb atom on the surface has nine 1NNs at mean distance 2.94 Å and two 2NNs at mean distance 3.76 Å, but in this case the 1NN varies in the range of 2.64 - 3.13 Å, while the Fe adatom is at 2.64 Å.

5. Electronic structure of the clean/doped Fe(100) surfaces plus Pb/Fe adatom

5.1. Clean Fe(100) surface plus adatom

Since the bond strengths of adatom can be correlated to the local density of PDOS at the Fermi level and to the number of empty states in D-bands [47,48], we analysed the PDOS of both Pb and Fe adatoms on T (Fig. SM5a and Fig. SM6a), B (Fig. SM5b and Fig. SM6b), and H adsorption sites (Figs. 1a and b) in order to compare the bond strengths of adatom on the Fe(100) iron surface. In our analysis we considered that the surface d-orbitals coupling gives trends in bonds energy and contributes to the bonding geometry [49]. The vanishing of the spin-down component of Pb's d-orbitals at the Fermi level in the H position (Fig. 1a; binding energy −3.73 eV) agrees with the fact that the adsorption in H is stronger than that at the top and bridge sites (Fig. SM5a, b; binding energy −2.83 eV and −3.14 eV, respectively) for which PDOS (E_F) is non-zero for both spin components, and therefore the systems are more reactive. The electron charge rearrangement is shown on the top of each panel in Fig. 1 and Fig. SM5. It is possible to observe that in the more stable configuration (H site), Pb adatom maximizes its number of bonds forming four bonds with iron surface, while Pb adatom in T and B sites, forms one and two bonds, respectively (Table 3). All the isosurfaces shown in the following figures (Figs. 1 and 3 and Figs. SM5-SM8) correspond to 10 % of the maximum value of the featured field.

PDOS(E_F) of Fe adatom d-orbitals has a peak for the T configuration (Fig. SM6a), this implies high reactivity and low stability. Indeed, the binding energy reaches its highest value (−1.68 eV), i.e. Fe adatom in T configuration compared to Fe adatom in H configuration is less bound of −1.93 eV. On the other hand, PDOS(E_F) of Fe adatom in H site (Fig. 1b) is very low, so that the surface is more stable and the adatom has the lowest binding energy (−3.61 eV). However, for the system with Fe-adatom on B site (Fig. SM6b), both the PDOS(E_F) of d-orbitals, and the binding energy, present intermediate values between those for T and H sites.

The s- and p-orbitals of Fe adatom are low in energy, and the coupling to the orbitals from the surface atoms gives a strong contribution to the total bond energy and a lesser contribution to the trends from one configuration to the next [50].

The charge density difference, reported on the top of each panel of Fig. 1b and Fig. SM6, shows that, in the H configuration, electrons

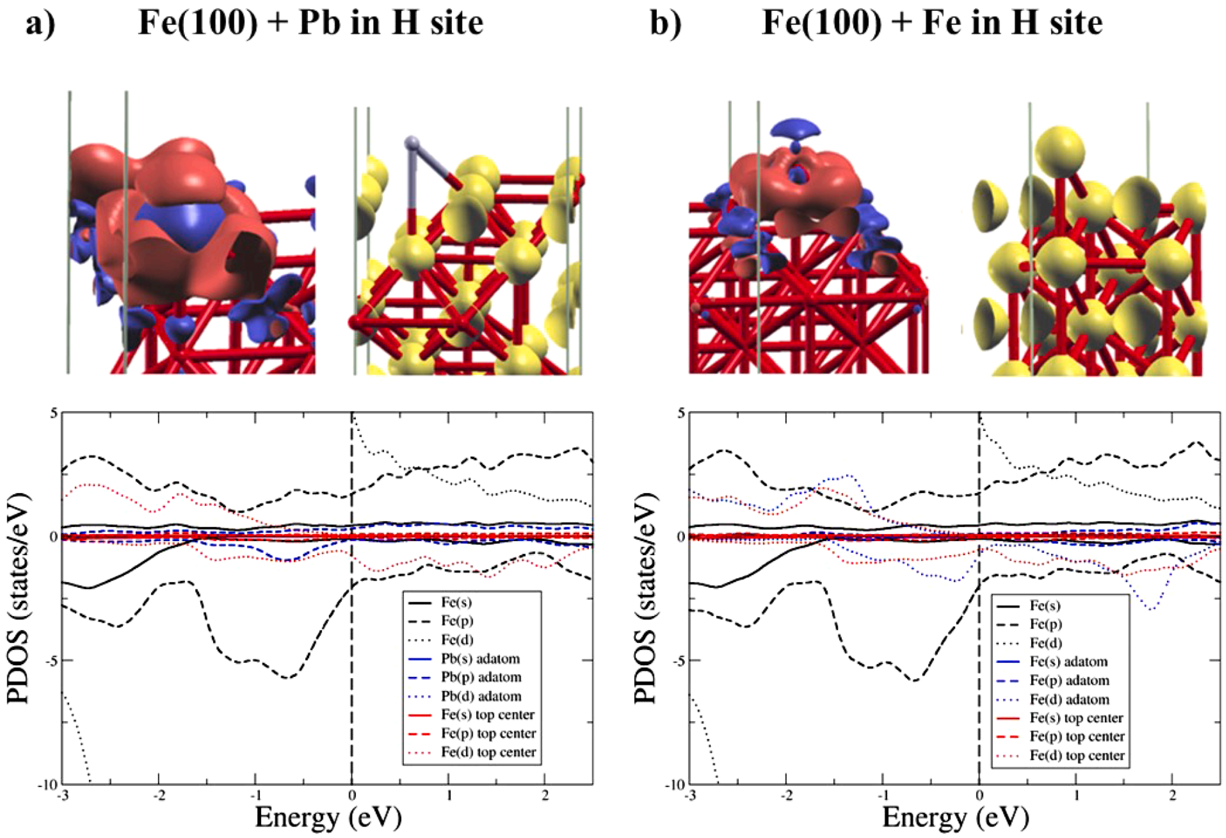

Fig. 1. Projected density of states of Pb (a) and Fe (b) adsorption on Fe(100) surface in hollow site. Dashed and dotted lines are used for s-, p- and d-orbitals, and black, blue and red lines indicate Fe atom, adatom and substituting atom (or Fe atom to be substituted), respectively. On the top of each panel the corresponding difference of charge density (on the left) and spin polarization (on the right) are shown (positive (negative) values are in red (blue), yellow is for only positive values). The isosurface values are set to 0.0015 *e* for the difference of charge density and to 0.12 *e* for the spin polarization.

rearrange to form four bonds between the Fe adatom and the four 1NNs Fe atoms, tending to recover the eight-fold coordination of Fe atoms in the bulk iron. In the T and B configurations, electron charge redistributes around the Fe adatom to form one and two bonds with the 1NNs Fe atom (s), respectively.

5.2. *Doped Fe(100) surfaces and doped Fe(100) surfaces plus adatom*

To analyse the PDOS of both Fe and Pb adatoms adsorbed on doped iron surface, we firstly compared the PDOS of the clean and doped iron surfaces. As shown in Fig. 2a the contribution to the total DOS of the top layer Fe atom in *S* position is separated from the others. This Fe atom is substituted by Pb, Cr or Ni atoms in the doped surfaces.

The PDOS of substitutional Pb is very low, the contributions from s- and p-orbitals at Fermi level replace the contributions from substituted Fe atom d-orbitals (Fig. 2b). The ᴅ-shell of Pb is full and the s- and p-orbitals of Pb are not as reactive as d-orbitals of Fe. Therefore, the surface reactivity decreases when Fe is substituted with Pb. Indeed, the binding energy of Fe (Pb) adatom increases from −3.61 (−3.73) to −2.99 (−3.19) eV with respect to adsorption on clean surface. The PDOS (E_F) not zero for Fe (Pb) adatom, indicates the reactivity of the adatom (Fig. SM7). The intensity of PDOS at Fermi level for substitutional Cr is comparable with that of the substituted Fe atom (Fig. 2c). The main difference is that spin-up and spin-down states are inverted, and this is evidenced by the anti-ferromagnetism of substitutional Cr. Therefore, Cr doping does not change the surface reactivity of iron. Indeed, the PDOSs and the binding energies of Fe(Pb) adatom on Fe(100)$_{Cr}$ and clean Fe (100) are similar (Fig. SM8).

PDOS of Fe(100)$_{Ni}$ is shown in Fig. 2d where we observe that PDOS (E_F) for substitutional Ni atom is increased, while the number of empty ᴅ-states is decreased with respect to substituted Fe. In this way the surface reactivity is increased. Nonetheless, when Fe atom is adsorbed on Fe(100)$_{Ni}$, PDOSs of substitutional Ni and Fe adatom, shown in Fig. 3a, are resonant at Fermi level so that the surface is stabilized. Therefore, the binding energy of Fe adatom decreases from −3.61 to −3.68 eV after Ni doping. The PDOS of Pb adatom on Fe(100)$_{Ni}$, shown in Fig. 3b, is quite low around Fermi level and not resonant. The reactive Ni doped surface is not stabilized by low reactive Pb adatom s- and p-orbitals and it remains more reactive than clean surface. This agrees with the binding energy value (−3.46 eV) calculated for the Pb adatom adsorbed on Fe(100)$_{Ni}$ that is greater than that of the Fe(100)$_{Pb}$ (−3.73 eV).

The total magnetization of the Ni, Cr and Pb doped surface is 2.59, 2.43 and 2.55 μB /atom, respectively. By analysing the spin polarization (top of Figs. 3, SM7 and SM8), it can be observed that the large decrease of magnetization for Cr doping (with respect to the total magnetization of 2.65 μB /atom for clean surface) is due to the anti-ferromagnetic behaviour of Cr, while Pb atom is not magnetic, and Ni atom is ferromagnetic. Indeed, the spin polarization of Pb is very low, and Ni has spin polarization lower than Fe atoms.

The spin polarization of Fe(Pb) adatom in the hollow site of the clean Fe(100) surface is 3.09 (−0.43) *e* (where *e* is the electron charge), while if Fe (Pb) atom is adsorbed on the hollow site of the Fe(100) surface doped with Ni, Pb, or Cr, is 3.18 (−0.36) *e*, 3.07 (−0.30) *e* and 2.93 (−0.33) *e*, respectively. Therefore, the effect of doping on adatom's magnetism is quite small.

6. Conclusions

Based on the first-principles calculations, we investigated the interaction between Pb adatom and the Fe(100) surface in different configurations. The results show that the hollow (H) site provides the most stable configurations of adsorbed Pb and Fe adatom on the clean Fe(100) surface, and that Fe(100)^{Pb} is always more stable than Fe(100)^{Fe} (the E_b^a values indicate that is more energetically favourable to have a Pb adatom on the iron surface rather than continue the slab with a Fe adatom). Moreover, in H position the adatom has the highest number of 1NNs at the lowest distances (in this configuration the adatom interacts with more atoms).

In addition, we found that, while the doping of the Fe(100) surface with Ni atom is an energetically favourable process ($\Delta E < 0$) and with the highest energy to remove it from the surface (the lowest E_b^s). On the contrary, the doping with Cr or Pb atom requires energy to be provided and these atoms are less bonded from the surface. Moreover, the Ni doping changes the order of the more stable adatom, since in the Fe (100)$_{Ni}$ the Fe adatom ($E_b^a = -3.68$ eV) is more bonded than the Pb one

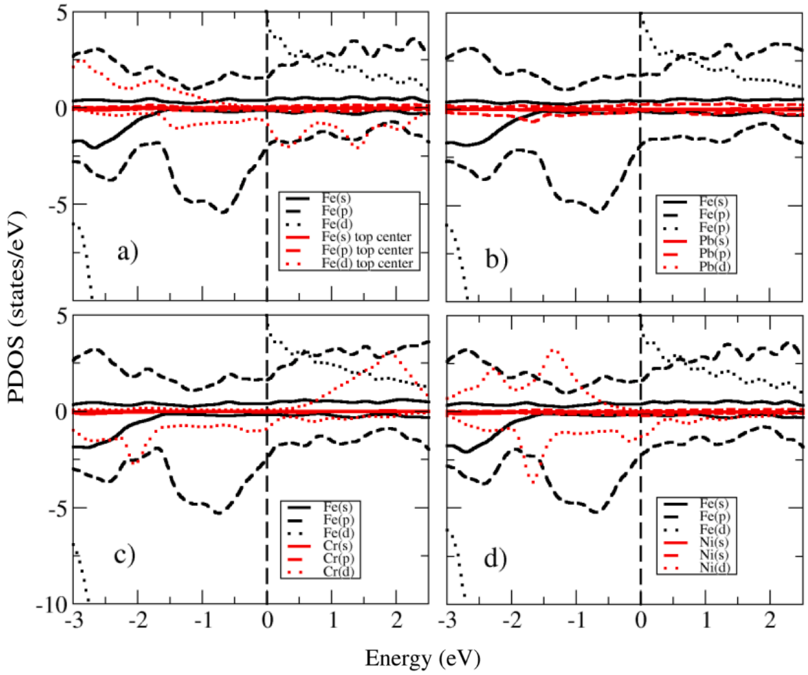

Fig. 2. Projected density of states of the clean and doped iron surfaces: Fe(100) (a), Fe(100)$_{Pb}$ (b), Fe(100)$_{Cr}$ (c), and Fe(100)$_{Ni}$ (d).

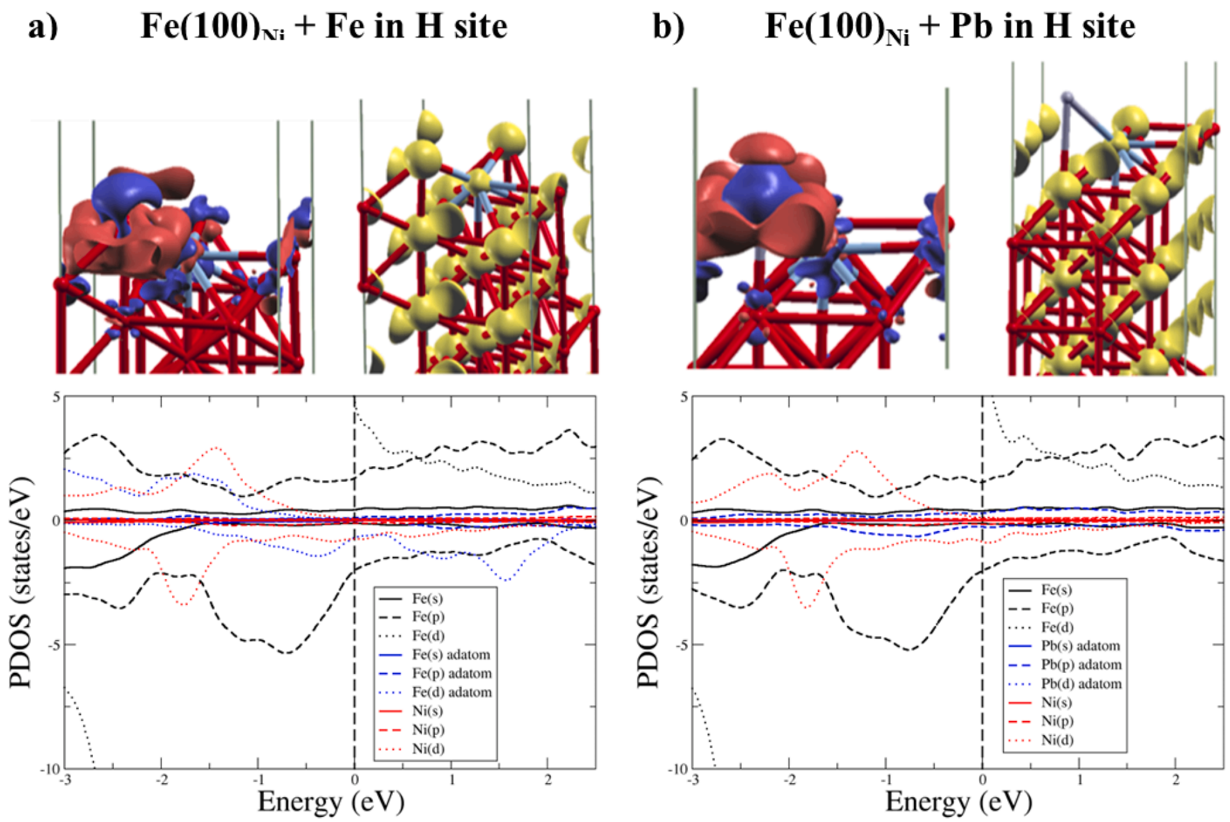

Fig. 3. Projected density of states of Fe (a) and Pb (b) adsorption in hollow site on Ni-doped Iron surface. Dashed and dotted lines are used for s-, p- and d-orbitals, and black, blue and red lines indicate Fe atom, adatom and substituting atom (or Fe atom to be substituted), respectively. On the top of each panel the corresponding difference of charge density (on the left) and spin polarization (on the right) are shown (positive (negative) values are in red (blue), yellow is for only positive values). The isosurface values are set to 0.004 and 0.002 *e* in a) and b), respectively, for the difference of charge density and to 0.12 *e* for the spin polarization.

($E_b^a = -3.46$ eV). The evaluations of the percentage change in inter-layer distances along the z-direction of the surface indicate that no significant differences were observed between the Δ_{ij} of Fe(100) doped with Cr or Ni, and the corresponding one of the clean Fe(100) surface. However, the presence of the alloying element causes an increase of ~ 1 % in the contraction of the outer layer with respect to the that observed for the clean Fe(100) surface. This is not true for Pb doping, in which there is an expansion of the external atoms ($\Delta_{12} = 7.9$ %) and an expansion of the fourth layer, $\Delta_{45} = +0.46$ %. The same trend is observed in the nearest neighbours analysis. An iron atom on the Fe(100) surface has four 1NN at 2.45 Å and five 2NN at 2.86 Å. These values are slightly changed in the Cr/Ni doping. In the former case the distance of the 1NN atoms is elongated to 2.47 Å in fact the Cr atom is above the iron surface. In the latter case the 1NN atoms are at 2.41 Å from the Ni atom, which is slightly lower than iron surface. On the contrary, the Pb substitution produces an increase of the number (eight) and distance (2.94 Å) of the 1NNs. Then, regarding the structural analysis, the presence of lead produces more evident deformation compared to the chromium and nickel doping.

The analysis of the PDOS of both Pb and Fe adatoms on T, B, and H adsorption sites of the clean Fe(100) surface has shown that the PDOS features at the Fermi energy capture the trends of the binding energy on the different adsorption sites, while the charge density difference agrees with the formation of bonds and the number of first-nearest neighbours.

For the doped iron surfaces, we found that the surface with substitutional Pb is less reactive than the clean surface, indeed the s- and p-orbitals at Fermi level of substitutional Pb are less reactive than d-orbitals of Fe. Moreover, the Cr doping does not change the surface reactivity of iron intensity, indeed the PDOS at Fermi level for substitutional Cr is found comparable with that of the substituted Fe atom, with the main difference that the spin-up and the spin-down states are inverted.

In contrast the PDOS(E_F), and the surface reactivity of Fe(100)$_{Ni}$ are increased. Indeed, for the system with Fe (Pb) adatom adsorbed on the Fe(100)$_{Ni}$, the analysis of the PDOS around Fermi level shows that the reactive d-orbitals of the substitutional Ni are stabilized by the Fe adatom and not stabilized by the Pb adatom. All these results agree with the trends of the binding energy. The analysis of spin polarization shows that the doping with Cr, Ni or Pb does not affect the magnetism of Fe (Pb) adatom on the Fe(100) surface.

In conclusion, lessons learnt are the following: the preferred position for the adatom is in the hollow site; Pb atoms produce larger structural distortions than Cr/Ni alloying; the Ni doping, that is energetically favourable, can hinder the corrosion process due to lead interactions. Indeed, the Fe adatom forms the most stable bond on the Ni doped surface.

CRediT authorship contribution statement

Simone Giuseppponi: Conceptualization, Software, Investigation, Data curation, Writing – original draft. **Francesco Buonocore:** Investigation, Software, Data curation, Writing – review & editing. **Barbara Ferrucci:** Validation, Writing – review & editing. **Massimo Celino:** Conceptualization, Validation, Supervision, Writing – review & editing.

Declaration of Competing Interest

The authors declare that they have no known competing financial interests or personal relationships that could have appeared to influence the work reported in this paper.

Data availability

Data will be made available on request.

Acknowledgments

The computing resources and the related technical support used for this work have been provided by CRESCO/ENEAGRID High Performance Computing infrastructure and its staff [51]. CRESCO/ENEAGRID High Performance Computing infrastructure is funded by ENEA, the Italian National Agency for New Technologies, Energy and Sustainable Economic Development and by Italian and European research projects, see http://www.cresco.enea.it/english for information. The authors acknowledge the extensive use of the ENEA FARO facility and the support of its management team [52].

Supplementary materials

Supplementary material associated with this article can be found, in the online version, at doi:10.1016/j.susc.2023.122402.

References

[1] M. Tarantino, M. Angiolini, S. Bassini, S. Cataldo, C. Ciantelli, C. Cristalli, A. Del Nevo, I. Di Piazza, D. Diamanti, M. Eboli, A. Fiore, G. Grasso, F. Lodi, P. Lorusso, R. Marinari, D. Martelli, F. Papa, C. Sartorio, M. Utili, A. Venturini, Overview on lead-cooled fast reactor design and related technologies development in ENEA, Energies (2021), https://doi.org/10.3390/en14165157, 14 5157.

[2] X. Huang, X. Gong, M. Song, Jiajun. Chen, Feiyu Hu, Yuan Yin, Jun Xiao, Hui Wang, Hao Wang, Haoran Gong, Yangbin Deng, Bo Pang, Yongchun Li, Liquid metal embrittlement susceptibility of a high-entropy alloy exposed to oxygen-depleted liquid lead-bismuth eutectic at 250 and 350 C, J. Nucl. Mater. 528 (2020), 151859, https://doi.org/10.1016/j.jnucmat.2019.151859.

[3] Z.Y. Wu, X. Zhao, Y. Liu, Y. Cai, J.Y. Li, H. Chen, Q. Wan, D. Yang, J. Tan, H.D. Liu, Y.M. Chen, J.L. Guo, J. Zhang, G.D. Zhang, Z.G. Li, B. Yang, Lead-bismuth eutectic (LBE) corrosion behavior of AlTiN coatings at 550 and 600°C, J. Nucl. Mater. 539 (2020), 152280, https://doi.org/10.1016/j.jnucmat.2020.152280.

[4] Jinsuo Zhang, Ning Li, Review of the studies on fundamental issues in LBE corrosion, J. Nucl. Mater. 373 (Issues 1–3) (2008) 351–377, https://doi.org/10.1016/j.jnucmat.2007.06.019.

[5] Jun Lim, Hyo On Nam, Il Soon Hwang, Ji Hyun Kim, A study of early corrosion behaviours of FeCrAl alloys in liquid lead-bismuth eutectic environments, J. Nucl. Mater. 407 (2010) 205, https://doi.org/10.1016/j.jnucmat.2010.10.018.

[6] Zunqi Xiao, Jing Liu, Zhizhong Jiang, Lin Luo, Corrosion behavior of refractory metals in liquid lead at 1000°C for 1000h, Nucl. Eng. Technol. 54 (2022) 1954, https://doi.org/10.1016/j.net.2021.12.014.

[7] Xing Gong, M.P. Short, T. Auger, E. Charalampopoulou, K. Lambrinou, Environmental degradation of structural materials in liquid lead- and lead-bismuth eutectic-cooled reactors, Prog. Mater. Sci. 12 (2022), https://doi.org/10.1016/j.pmatsci.2022.100920, 100920.

[8] D. Frazer, E. Stergar, C. Cionea, P. Hosemann, Liquid metal as a heat transport fluid for thermal solar power applications, Energy Procedia 49 (2014) 627, https://doi.org/10.1016/j.egypro.2014.03.068.

[9] J. Pacio, A. Fritsch, C. Singer, R. Uhlig, Liquid metals as efficient coolants for high-intensity point-focus receivers: implications to the design and performance of next-generation CSP systems, Energy Procedia 49 (2014) 647, https://doi.org/10.1016/j.egypro.2014.03.070.

[10] N. Lorenzin, A. Abanades, A review on the application of liquid metals as heat transfer fluid in concentrated solar power technologies, Int. J. Hydrogen Energy 41 (2016) 6990, https://doi.org/10.1016/j.ijhydene.2016.01.030.

[11] T. Conroy, M.N. Collins, J. Fisher, R. Grimes, Thermohydraulic analysis of single phase heat transfer fluids in CSP solar receivers, Renew. Energy 129 (2018) 150, https://doi.org/10.1016/j.renene.2018.05.101.

[12] J. Guo, X. Huai, K. Cheng, The comparative analysis on thermal storage systems for solar power with direct steam generation, Renew. Energy 115 (2018) 217, https://doi.org/10.1016/j.renene.2017.08.046.

[13] A. Rinaldi, G. Barbieri, E. Kosykh, P. Szakalos, C. Testani, Materials for high temperature liquid lead storage for concentrated solar power (CSP) air tower systems, Materials 14 (2021) 3261, https://doi.org/10.3390/ma14123261.

[14] Song Chi, Li Dong-Dong, Xu Yi-Chung, Pan Bi-Cai, Liu Chang-Song, Wang Zhi-Guang, Corrosion related properties of iron (100) surface in liquid lead and bismuth environments: a first-principles study, Chin. Phys. B 23 (2014), 056801, https://doi.org/10.1088/1674-1056/23/5/056801.

[15] Y. Xu, C. Song, Y. Zhang, C.S. Liu, B.C. Pan, Z. Wang, An energetic evaluation of dissolution corrosion capabilities of liquid metals on iron surface, Phys. Chem. Chem. Phys. 16 (2014) 16837, https://doi.org/10.1039/c4cp01224k.

[16] P. Giannozzi, S. Baroni, N. Bonini, M. Calandra, R. Car, C. Cavazzoni, D. Ceresoli, G.L. Chiarotti, M. Cococcioni, I. Dabo, A. Dal Corso, S. Fabris, G. Fratesi, S. de Gironcoli, R. Gebauer, U. Gerstmann, C. Gougoussis, A. Kokalj, M. Lazzeri, L. Martin-Samos, N. Marzari, F. Mauri, R. Mazzarello, S. Paolini, A. Pasquarello, L. Paulatto, C. Sbraccia, S. Scandolo, G. Sclauzero, A.P. Seitsonen, A. Smogunov, P. Umari, R.M. Wentzcovitch, QUANTUM ESPRESSO: a modular and open-source software project for quantum simulations of materials, J. Phys. 21 (2009), 395502, https://doi.org/10.1088/0953-8984/21/39/395502.

[17] P. Giannozzi, O. Andreussi, T. Brumme, O. Bunau, M. Buongiorno Nardelli, M. Calandra, R. Car, C. Cavazzoni, D. Ceresoli, M. Cococcioni, N. Colonna, I. Carnimeo, A. Dal Corso, S. de Gironcoli, P. Delugas, R.A. DiStasio Jr, A. Ferretti, A. Floris, G. Fratesi, G. Fugallo, R. Gebauer, U. Gerstmann, F. Giustino, T. Gorni, J. Jia, M. Kawamura, H.Y. Ko, A. Kokalj, E. Küçükbenli, M. Lazzeri, M. Marsili, N. Marzari, F. Mauri, N.L. Nguyen, H.V. Nguyen, A. Otero-de-la-Roza, L. Paulatto, S. Poncé, D. Rocca, R. Sabatini, B. Santra, M. Schlipf, A.P. Seitsonen, A. Smogunov, I. Timrov, T. Thonhauser, P. Umari, N. Vast, X. Wu, S. Baroni, Advanced capabilities for materials modelling with Quantum ESPRESSO, J. Phys. 29 (2017), 465901, https://doi.org/10.1088/1361-648X/aa8f79.

[18] P. Hohenberg, W. Kohn, Inhomogeneous electron gas, Phys. Rev. 136 (1964), https://doi.org/10.1103/PhysRev.136.B864. B864.

[19] W. Kohn, L.J. Sham, Self-consistent equations including exchange and correlation effects, Phys. Rev. 140 (1965) A1133, https://doi.org/10.1103/PhysRev.140.A1133.

[20] D. Vanderbilt, Soft self-consistent pseudopotentials in a generalized eigenvalue formalism, Phys. Rev. B 41 (1990) 7892, https://doi.org/10.1103/PhysRevB.41.7892.

[21] K. Laasonen, R. Car, C. Lee, D. Vanderbilt, Implementation of ultrasoft pseudopotentials in ab initio molecular dynamics, Phys. Rev. B 43 (1991) 6796, https://doi.org/10.1103/PhysRevB.43.6796.

[22] K. Laasonen, A. Pasquarello, C. Lee, R. Car, D. Vanderbilt, Car-Parrinello molecular dynamics with Vanderbilt ultrasoft pseudopotentials, Phys. Rev. B 47 (1993) 10142, https://doi.org/10.1103/PhysRevB.47.10142.

[23] J.P. Perdew, K. Burke, M. Ernzerhof, Generalized gradient approximation made simple, Phys. Rev. Lett. 77 (1996) 3865, https://doi.org/10.1103/PhysRevLett.77.3865.

[24] H.J. Monkhorst, J.D. Pack, Special points for Brillouin-zone integrations, Phys. Rev. B 13 (1976) 5188, https://doi.org/10.1103/PhysRevB.13.5188.

[25] N. Marzari, D. Vanderbilt, A. De Vita, M.C. Payne, Thermal contraction and disordering of the Al(110) surface, Phys. Rev. Lett. 82 (1999) 3296, https://doi.org/10.1103/PhysRevLett.82.3296.

[26] W.R. Tyson, R.A. Ayres, D.F. Stein, Anisotropy of cleavage in B.C.C. transition metals, Acta Metall. 21 (1973) 621, https://doi.org/10.1016/0001-6160(73)90071-0.

[27] A. Hung, I. Yarovsky, J. Muscat, S. Russo, I. Snook, R.O. Watts, First-principles study of metallic iron interfaces, Surf. Sci. 501 (2002) 261, https://doi.org/10.1016/S0039-6028(01)01762-9.

[28] L. Bengtsson, Dipole correction for surface supercell calculations, Phys. Rev. B 59 (1999) 12301, https://doi.org/10.1103/PhysRevB.59.12301.

[29] V. Fiorentini, M. Methfessel, Extracting convergent surface energies from slab calculations, J. Phys. 8 (1996) 6525, https://doi.org/10.1088/0953-8984/8/36/005.

[30] N.E. Singh-Miller, N. Marzari, Surface energies, work functions, and surface relaxations of low-index metallic surfaces from first principles, Phys. Rev. B 80 (2009), 235407, https://doi.org/10.1103/PhysRevB.80.235407.

[31] M.J. Mehl, J.E. Osburn, D.A. Papaconstantopoulos, B.M. Klein, Structural properties of ordered high-melting-temperature intermetallic alloys from first-principles total-energy calculations, Phys. Rev. B 41 (1990) 10311, https://doi.org/10.1103/PhysRevB.41.10311.

[32] H.M. Ledbetter, R.P. Leed, Elastic properties of metals and alloys, I. Iron, nickel, and iron-nickel alloys, J. Phys. Chem. Ref. Data 2 (1973) 531, https://doi.org/10.1063/1.3253127.

[33] J.J. Adams, D.S. Agosta, R.G. Leisure, H. Ledbetter, Elastic constants of monocrystal iron from 3 to 500K, J. Appl. Phys. 100 (2006), 113530, https://doi.org/10.1063/1.2365714.

[34] B.J. Lee, M.I. Baskes, H. Kim, Y.K. Cho, Second nearest-neighbor modified embedded atom method potentials for bcc transition metals, Phys. Rev. B 64 (2010), 184102, https://doi.org/10.1103/PhysRevB.64.184102.

[35] T. Shimada, Y. Ishii, T. Kitamura, Ab initio study of magnetism at iron surfaces under epitaxial in-plane strain, Phys. Rev. B 81 (2010), 134420, https://doi.org/10.1103/PhysRevB.81.134420.

[36] A.F. Bialon, T. Hammerschmidt, R. Drautz, Ab initio study of boron in α-iron: migration barriers and interaction with point defects, Phys. Rev. B 87 (2013), 104109, https://doi.org/10.1103/PhysRevB.87.104109.

[37] L. Rena, Y. Chenga, R. Shaob, X. Mengc, J. Yanga, Q. Wanga, DFT studies of adsorption properties and bond strengths of H_2S, HCN and NH_3 on Fe(1 0 0), Appl. Surf. Sci 500 (2020), 144232, https://doi.org/10.1016/j.apsusc.2019.144232.

[38] A. Stibor, G. Kresse, A. Eichler, J. Hafner, Density functional study of the adsorption of CO on Fe(1 1 0), Surf. Sci. 507 (2002), https://doi.org/10.1016/S0039-6028(02)01182-2. -510 99.

[39] P. Błoński, A. Kiejna, Structural, electronic, and magnetic properties of bcc iron surfaces, Surf. Sci. 601 (2007) 123, https://doi.org/10.1016/j.susc.2006.09.013.

[40] L. Vitos, A.V. Ruban, H.L. Skriver, J. Kollar, The surface energy of metals, Surf. Sci. 411 (1998) 186, https://doi.org/10.1016/S0039-6028(98)00363-X.

[41] M.J.S. Spencer, A. Hung, I.K. Snook, I. Yarovsky, Density functional theory study of the relaxation and energy of iron surfaces, Surf. Sci. 513 (2002) 389, https://doi.org/10.1016/S0039-6028(02)01809-5.

[42] A. Chakrabartya, E.T. Bentriab, S.A. Omotayoc, O. Bouhalic, N. Mousseaud, C. S. Becquarte, F.E. Mellouhi, Elucidating the role of extended surface defects at Fe

surfaces on CO adsorption and dissociation, Appl. Surf. Sci. 491 (2019) 792, https://doi.org/10.1016/j.apsusc.2019.05.278.

[43] Z.Q. Wang, Y.S. Li, F. Jona, P.M. Marcus, Epitaxial growth of body-centered-cubic nickel on iron, Solid State Commun. 623 (1987) 61, https://doi.org/10.1016/0038-1098(87)90374-7.

[44] K.O. Legg, F. Jona, D.W. Jepsen, P.M. Marcus, Low-energy electron diffraction analysis of clean Fe (001), J. Phys. C 10 (1977) 937, https://doi.org/10.1088/0022-3719/10/7/005.

[45] M. Benoit, C. Langlois, N. Combe, H. Tang, M.J. Casanove, Structural and electronic properties of the Au(001)/Fe(001) interface from density functional theory calculations, Phys. Rev. B 86 (2012), 075460, https://doi.org/10.1103/PhysRevB.86.075460.

[46] S.G. Nelson, M.J.S. Spencer, I.K. Snook, I. Yarovsky, Effect of S contamination on properties of Fe(100) surfaces, Surf. Sci. 590 (2005) 63, https://doi.org/10.1016/j.susc.2005.06.014.

[47] M.H. Cohen, M.V. Ganduglia-Pirovano, J. Kudrnovsky, Orbital symmetry, reactivity, and transition metal surface chemistry, Phys. Rev. Lett. 72 (1994) 3222, https://doi.org/10.1103/PhysRevLett.72.3222.

[48] M.H. Cohen, M.V. Ganduglia-Pirovano, Electronic and nuclear chemical reactivity, J. Chem. Phys. 101 (1994) 8988, https://doi.org/10.1063/1.468026.

[49] J. Harris, S. Andersson, H_2 dissociation at metal surfaces, Phys. Rev. Lett. 55 (1985) 1583, https://doi.org/10.1103/PhysRevLett.55.1583.

[50] B. Hammer, J.K. Nørskov, Theory of Adsorption and Surface Reactions (1997) 285–351.

[51] Iannone et al. CRESCO ENEA HPC clusters: a working example of a multifabric GPFS Spectrum Scale Layout. International Conference on High Performance Computing & Simulation (HPCS), Dublin, Ireland, (2019) 1051. 10.1109/HPCS48598.2019.9188135.

[52] Fast access to remote objects 2.0. A renewed gateway to ENEAGRID distributed computing resources, FGCS 94 (2019) 920, https://doi.org/10.1016/j.future.2017.11.032.